

All-optical osteotomy to create windows for transcranial imaging in mice

Diana C. Jeong,¹ Philbert S. Tsai¹ and David Kleinfeld^{1,2}

¹Department of Physics, 9500 Gilman Drive, University of California, San Diego, La Jolla, CA 92093 USA.

²Section of Neurobiology, 9500 Gilman Drive, University of California, San Diego, La Jolla, CA 92093 USA.

*dk@physics.ucsd.edu

Abstract: Surgical procedures as a prelude to optical imaging are a rate-limiting step in experimental neuroscience. Towards automation of these procedures, we describe the use of nonlinear optical techniques to create a thinned skull window for transcranial imaging. Metrology by second harmonic generation was used to map the surfaces of the skull and define a cutting path. Plasma-mediated laser ablation was utilized to cut bone. Mice prepared with these techniques were used to image subsurface cortical vasculature and blood flow. The viability of the brain tissue was confirmed via histological analysis and supports the utility of solely optical techniques for osteotomy and potentially other surgical procedures.

©2013 Optical Society of America

OCIS codes: (170.0170) Medical optics and biotechnology; (120.0120) Instrumentation, measurement, and metrology; (180.0180) Microscopy.

References and links

1. W. Denk, J. H. Strickler, and W. W. Webb, "Two-photon laser scanning fluorescence microscopy," *Science* **248**(4951), 73–76 (1990).
2. F. Helmchen and W. Denk, "Deep tissue two-photon microscopy," *Nat. Methods* **2**(12), 932–940 (2005).
3. P. J. Drew, A. Y. Shih, J. D. Driscoll, P. M. Knutsen, P. Blinder, D. Davalos, K. Akassoglou, P. S. Tsai, and D. Kleinfeld, "Chronic optical access through a polished and reinforced thinned skull," *Nat. Methods* **7**(12), 981–984 (2010).
4. K. Svoboda, W. Denk, D. Kleinfeld, and D. W. Tank, "*In vivo* dendritic calcium dynamics in neocortical pyramidal neurons," *Nature* **385**(6612), 161–165 (1997).
5. H. T. Xu, F. Pan, G. Yang, and W. B. Gan, "Choice of cranial window type for *in vivo* imaging affects dendritic spine turnover in the cortex," *Nat. Neurosci.* **10**(5), 549–551 (2007).
6. A. Holtmaat, T. Bonhoeffer, D. K. Chow, J. Chuckowree, V. De Paola, S. B. Hofer, M. Hübener, T. Keck, G. Knott, W. C. Lee, R. Mostany, T. D. Mrsic-Flogel, E. Nedivi, C. Portera-Cailliau, K. Svoboda, J. T. Trachtenberg, and L. Wilbrecht, "Long-term, high-resolution imaging in the mouse neocortex through a chronic cranial window," *Nat. Protoc.* **4**(8), 1128–1144 (2009).
7. B. J. Schaller, R. Gruber, H. A. Merten, T. M. A. Kruschat, H. M. D. Schliephake, M. Buchfelder, and H. C. Ludwig, "Piezoelectric bone surgery: A revolutionary technique for minimally invasive surgery in cranial base and spinal surgery? Technical note," *Neurosurgery* **57**(Suppl.4), E410, discussion E410 (2005).
8. R. D. Piper, G. A. Lambert, and J. W. Duckworth, "Cortical blood flow changes during spreading depression in cats," *Am. J. Physiol.* **261**(1 Pt 2), H96–H102 (1991).
9. A. Arieli, A. Grinvald, and H. Slovin, "Dural substitute for long-term imaging of cortical activity in behaving monkeys and its clinical implications," *J. Neurosci. Methods* **114**(2), 119–133 (2002).
10. R. B. Boyd, *Nonlinear Optics, Second Edition* (Academic Press, 2004).
11. Y. Guo, P. P. Ho, H. Savage, D. Harris, P. Sacks, S. Schantz, F. Liu, N. Zhadin, and R. R. Alfano, "Second-harmonic tomography of tissues," *Opt. Lett.* **22**(17), 1323–1325 (1997).
12. R. W. Terhune, P. D. Maker, and C. M. Savage, "Optical harmonic generation in calcite," *Phys. Rev. Lett.* **8**(10), 404–406 (1962).
13. P. J. Campagnola, M. D. Wei, A. Lewis, and L. M. Loew, "High-resolution nonlinear optical imaging of live cells by second harmonic generation," *Biophys. J.* **77**(6), 3341–3349 (1999).
14. A. Vogel and V. Venugopalan, "Mechanisms of pulsed laser ablation of biological tissues," *Chem. Rev.* **103**(2), 577–644 (2003).
15. S. I. Mian and R. M. Shtein, "Femtosecond laser-assisted corneal surgery," *Curr. Opin. Ophthalmol.* **18**(4), 295–299 (2007).
16. S. H. Chung and E. Mazur, "Surgical applications of femtosecond lasers," *J. Biophotonics* **2**(10), 557–572 (2009).
17. H. K. Soong, S. Mian, O. Abbasi, and T. Juhasz, "Femtosecond laser-assisted posterior lamellar keratoplasty: Initial studies of surgical technique in eye bank eyes," *Ophthalmology* **112**(1), 44–49 (2005).

18. P. S. Tsai, P. Blinder, B. J. Miglioni, J. Neev, Y. Jin, J. A. Squier, and D. Kleinfeld, "Plasma-mediated ablation: An optical tool for submicrometer surgery on neuronal and vascular systems," *Curr. Opin. Biotechnol.* **20**(1), 90–99 (2009).
19. M. Farid and R. F. Steinert, "Femtosecond laser-assisted corneal surgery," *Curr. Opin. Ophthalmol.* **21**(4), 288–292 (2010).
20. A. P. Joglekar, H. H. Liu, E. Meyhöfer, G. Mourou, and A. J. Hunt, "Optics at critical intensity: Applications to nanomorphing," *Proc. Natl. Acad. Sci. U.S.A.* **101**(16), 5856–5861 (2004).
21. B. C. Stuart, M. D. Feit, A. M. Rubenchik, B. W. Shore, and M. D. Perry, "Laser-induced damage in dielectrics with nanosecond to subpicosecond pulses," *Phys. Rev. Lett.* **74**(12), 2248–2251 (1995).
22. F. H. Loesel, M. H. Niemz, J. F. Bille, and T. Juhasz, "Laser-induced optical breakdown on hard and soft tissues and its dependence on the pulse duration: Experiment and model," *IEEE J. Quantum Electron.* **32**(10), 1717–1722 (1996).
23. W. B. Armstrong, J. A. Neev, L. B. Da Silva, A. M. Rubenchik, and B. C. Stuart, "Ultrashort pulse laser ossicular ablation and stapedotomy in cadaveric bone," *Lasers Surg. Med.* **30**(3), 216–220 (2002).
24. Y. Liu and M. Niemz, "Ablation of femoral bone with femtosecond laser pulses--A feasibility study," *Lasers Med. Sci.* **22**(3), 171–174 (2007).
25. D. N. Vitek, D. E. Adams, A. Johnson, P. S. Tsai, S. Backus, C. G. Durfee, D. Kleinfeld, and J. A. Squier, "Temporally focused femtosecond laser pulses for low numerical aperture micromachining through optically transparent materials," *Opt. Express* **18**(17), 18086–18094 (2010).
26. D. C. Jeong, P. S. Tsai, and D. Kleinfeld, "Prospect for feedback guided surgery with ultra-short pulsed laser light," *Curr. Opin. Neurobiol.* **22**(1), 24–33 (2012).
27. P. S. Tsai, B. Friedman, A. I. Ifarraguerri, B. D. Thompson, V. Lev-Ram, C. B. Schaffer, Q. Xiong, R. Y. Tsien, J. A. Squier, and D. Kleinfeld, "All-optical histology using ultrashort laser pulses," *Neuron* **39**(1), 27–41 (2003).
28. P. S. Tsai and D. Kleinfeld, "In vivo two-photon laser scanning microscopy with concurrent plasma-mediated ablation: Principles and hardware realization," in *Methods for In Vivo Optical Imaging, 2nd edition*, R. D. Frostig, Ed. (CRC Press, 2009), p. 59–115.
29. A. Y. Shih, J. D. Driscoll, P. J. Drew, N. Nishimura, C. B. Schaffer, and D. Kleinfeld, "Two-photon microscopy as a tool to study blood flow and neurovascular coupling in the rodent brain," *J. Cereb. Blood Flow Metab.* **32**(7), 1277–1309 (2012).
30. D. Kleinfeld, P. P. Mitra, F. Helmchen, and W. Denk, "Fluctuations and stimulus-induced changes in blood flow observed in individual capillaries in layers 2 through 4 of rat neocortex," *Proc. Natl. Acad. Sci. U.S.A.* **95**(26), 15741–15746 (1998).
31. P. J. Drew, P. Blinder, G. Cauwenberghs, A. Y. Shih, and D. Kleinfeld, "Rapid determination of particle velocity from space-time images using the Radon transform," *J. Comput. Neurosci.* **29**(1-2), 5–11 (2010).
32. J. E. W. Mayhew, S. Askew, Y. Zheng, J. Porcill, G. W. M. Westby, P. Redgrave, D. M. Rector, and R. M. Harper, "Cerebral vasomotion: 0.1 Hz oscillation in reflectance imaging of neural activity," *Neuroimage* **4**(3), 183–193 (1996).
33. N. Nishimura, C. B. Schaffer, B. Friedman, P. S. Tsai, P. D. Lyden, and D. Kleinfeld, "Targeted insult to individual subsurface cortical blood vessels using ultrashort laser pulses: three models of stroke," *Nat. Methods* **3**(2), 99–108 (2006).
34. N. Latov, G. Nilaver, E. A. Zimmerman, W. G. Johnson, A.-J. Silverman, R. Defendini, and L. Cote, "Fibrillary astrocytes proliferate in response to brain injury," *Dev. Biol.* **72**(2), 381–384 (1979).
35. R. J. Mullen, C. R. Buck, and A. M. Smith, "NeuN, a neuronal specific nuclear protein in vertebrates," *Development* **116**(1), 201–211 (1992).
36. D. A. Dawson and J. M. Hallenbeck, "Acute focal ischemia-induced alterations in MAP2 immunostaining: Description of temporal changes and utilization as a marker for volumetric assessment of acute brain injury," *J. Cereb. Blood Flow Metab.* **16**(1), 170–174 (1996).
37. D. Oron and Y. Silberberg, "Spatiotemporal coherent control using shaped, temporally focused pulses," *Opt. Express* **13**(24), 9903–9908 (2005).
38. C. B. Schaffer, N. Nishimura, E. N. Glezer, A. M. T. Kim, and E. Mazur, "Dynamics of femtosecond laser-induced breakdown in water from femtoseconds to microseconds," *Opt. Express* **10**(3), 196–203 (2002).
39. K. E. Sheetz, E. E. Hoover, R. Carriles, D. Kleinfeld, and J. A. Squier, "Advancing multifocal nonlinear microscopy: Development and application of a novel multibeam Yb:KGd(WO₄)₂ oscillator," *Opt. Express* **16**(22), 17574–17584 (2008).
40. J. J. Field, K. E. Sheetz, E. V. Chandler, E. E. Hoover, M. D. Young, S.-Y. Ding, A. W. Sylvester, D. Kleinfeld, and J. A. Squier, "Differential multiphoton laser-scanning microscopy," *IEEE J. Sel. Top. Quantum Electron.* **18**(1), 14–28 (2012).
41. E. M. Maynard, C. T. Nordhausen, and R. A. Normann, "The Utah intracortical Electrode Array: a recording structure for potential brain-computer interfaces," *Electroencephalogr. Clin. Neurophysiol.* **102**(3), 228–239 (1997).
42. A. N. Zorzos, J. Scholvin, E. S. Boyden, and C. G. Fonstad, "Three-dimensional multiwaveguide probe array for light delivery to distributed brain circuits," *Opt. Lett.* **37**(23), 4841–4843 (2012).
43. E. L. Gurevich and R. Hergenröder, "Femtosecond laser-induced breakdown spectroscopy: Physics, applications, and perspectives," *Appl. Spectrosc.* **61**(10), 233A–242A (2007).
44. B. M. Kim, M. D. Feit, A. M. Rubenchik, B. M. Mammini, and L. B. Da Silva, "Optical feedback signal for ultrashort laser-pulse ablation of tissue," *Appl. Surf. Sci.* **127–129**, 857–862 (1998).

1. Introduction

Optical imaging techniques provide a powerful and increasingly popular means to probe neuronal function in the mammalian central nervous system. A broad class of methods, including two-photon laser scanning microscopy [1], rely on the ability to achieve a diffraction limited focus deep within the preparation [2]. The supporting bone must be either thinned [3] or entirely removed [4] to reduce scattering and aberration of the incident beam [5]. As the skull and spinal vertebra are tightly juxtaposed with neuronal tissue, a critical issue during osteotomy is to minimize disruption of underlying neural tissue.

Current techniques to remove bone in experimental animals involve the use of mechanical tools, such as rotary drills and burrs [6] or more recently ultrasonic tips [7]. These surgical procedures are manually performed. Feedback on the extent of bone removal is largely unavailable and the neural tissue is potentially exposed to pressure and heat from the cutting process. Thus the surgical outcome relies on the skill of the surgeon. This may lead to inconsistencies among preparations and result in physiological dysfunction that includes spreading depression [8] and changes in the geometry of blood vessels [9] and neuronal processes [5]. As a means to ameliorate these complications, we seek an automated and non-mechanical procedure for osteotomy.

One aspect of automated laser surgery involves optical-based metrology to profile the surface and estimate the thickness of the bone. The generation of second harmonic light, produced when an ultrashort laser pulse interacts with a sample that is non-centrosymmetric [10], can be used for this purpose [11]. Bone exhibits strong second harmonic generation (SHG) as a consequence of the high content of collagen fibrils [12]. The second harmonic light is generated in the forward direction, yet back-scattering by the bone and underlying soft tissue allows the SHG signal to be detected by the incident beam optics and thus makes SHG a suitable technique for profiling the skull. The quadratic dependence of the amplitude of SHG on the amplitude of the pumping laser radiation enables optical sectioning and the bone can be probed along the optical axis with diffraction-limited resolution [13].

A second aspect of automated surgery concerns a means to either remove or thin the bone without the use of mechanical tools. Plasma-mediated laser ablation via ultrashort pulsed laser light [14–19] provides a way to remove material in highly localized volumes at the focus of the laser beam, a volume on the order of 0.1 to 10 μm^3 [20]. This process leads to ionization of the material and the creation of plasma at the focus of the laser beam. The requisite electric field is achieved with an ultrashort pulse with a width ~ 100 fs and a fluence ~ 1 J/cm². The ionized material in the immediate vicinity of the focal volume is ablated. Heat transfer to nearby regions of the material, which lowers the threshold for ablation, is minimized because the energy of the pulse is deposited in a time that is short compared to the rate of heat transfer away from the focus [21, 22]. Thus the use of ultrashort laser pulses minimizes collateral damage. Past work has demonstrated that cadaver bone may be precisely cut with plasma-mediated laser ablation [23–25] and motivates the present study on living tissue.

Here we ask if an automated surgical procedure, which avoids the use of mechanical tools but rather utilizes SHG for metrology and plasma-mediated laser ablation for the controlled removal of bone, is a viable means for osteotomy [26]. Our test bed is the fabrication of a thinned skull transcranial window in mice [3], with the goal of utilizing such windows for *in vivo* imaging of labeled brain vasculature and functional imaging of the underlying blood flow.

2. Experimental setup

The fabrication of a thinned skull window is performed through cycles of SHG metrology and laser ablation (Fig. 1(a)). The sample stage and optomechanics are based on a set-up used for the ablation and imaging of neuronal tissue [27, 28]. The oscillator, used for second harmonic generation, was tuned to $\lambda = 800$ nm. The amplified laser light, used for ablation, was supplied by a regenerative amplifier. The metrology and ablation beams share the optical axis. We use a 40-times magnification dipping objective to deliver and collect light; dichroic and

band-pass filters were selected for second harmonic detection of $\lambda = 400$ nm light. The cyclic process is under computer control (Fig. 1(b)). The care, experimental manipulation, and functional imaging of our mice followed standard procedures [29] that have been approved by the Institutional Animal Care and Use Committee at the University of California at San Diego.

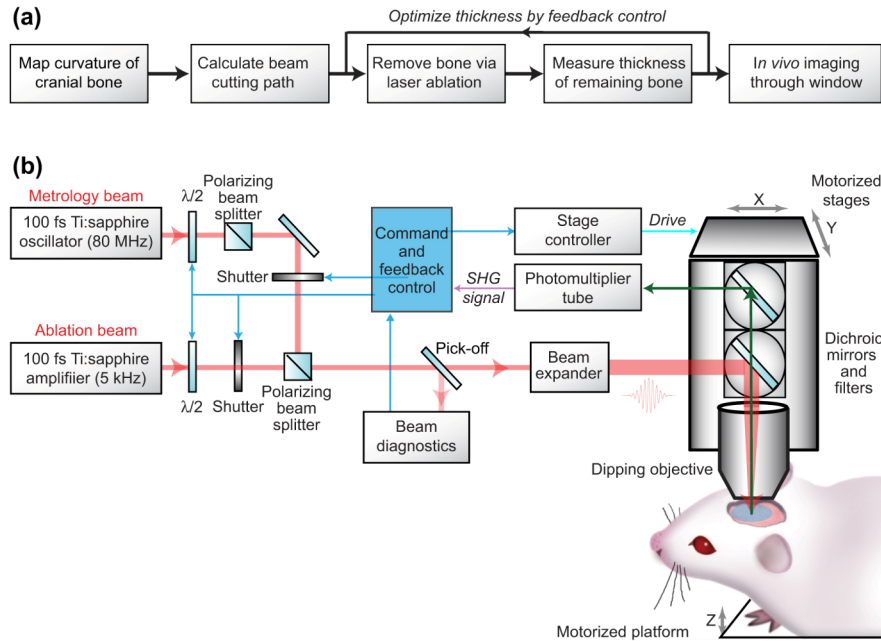


Fig. 1. Flow chart and schematic of the experimental set-up. (a) Procedures to produce a thinned skull window for transcranial imaging in mice. (b) Schematic of the set-up. An ultrashort pulsed Ti:sapphire oscillator (Mira HP pumped by a Verdi V18; Coherent, Inc.) is used for metrology of the skull based on the detection (H7422-40; Hamamatsu) of second harmonic light. A Ti:sapphire regeneratively amplified laser system (Libra, Coherent Inc.) is used as the source for the laser ablation. The two beams share the optical axis and are merged with a polarizing beam splitter placed before the water dipping objective (LUMPLANFL IR 40X 0.80 NA; Olympus). Translational stages (XYR-6060; Danaher) were used to scan incoming optical beam in X- and Y-directions. A third stage was used to move the preparation along the optical axis, *i.e.*, Z-direction (LMB-600; Danaher). The intensity of the metrology and ablation laser beams were controlled with half-wave plates followed by a polarizing beam splitter; the plates were coupled to a stepper motor and rotated for the desired intensity. The entire procedure is under control of a computer algorithm that operated the shutters (LS3; Uniblitz) and the stage controller (DMC-4040; Galil) and synchronized the data acquisition (NI 6110; National Instruments).

3. Second harmonic generation metrology

As the skull is curved, thinning must follow the surface to obtain a uniform thickness across the final transcranial window. Toward this goal, SHG metrology is used to map the height of the skull across the area of interest. This data is processed to direct control of motorized stages that translate the preparation and objective in the ablation process. Bone is typically removed in 8 μ m thick layers. Cycles of SHG metrology are intermixed with laser ablation until the desired thickness is achieved (Fig. 1(b)).

The second harmonic generation signal at a given location is measured as a function of the axial position of the focus, *i.e.*, the Z-direction (Fig. 2). We calibrated these measurements with data from isolated skulls. As the focus of the incident beam enters the top surface, the SHG signal was observed to rapidly increase to a maximum value (Fig. 2(a)). The signal then decays approximately exponentially as the focus was further lowered, presumably due to

multiple scattering events in the bone. The half-maximal position on the rising edge defines the absolute height of the front surface of the skull at a particular lateral position. The full-width-at-half-maximum of the SHG signal provides a lower limit on the thickness of the skull. However, the SHG signal is observed to exhibit a sharp drop in intensity as the focus is lowered past the bottom surface of the skull once it is thinner than $\sim 50\ \mu\text{m}$. This provides a means to gauge the thickness of the skull near the completion of the thinning processes.

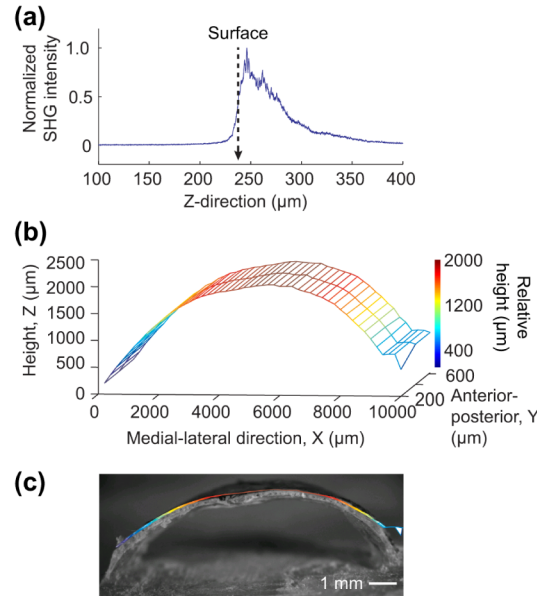


Fig. 2. Height and thickness of the skull as measured via second harmonic generation. (a) Intact bone was scanned along the Z-direction with ultrashort pulsed laser light. The signal rapidly increased as the focus approached the surface of the skull. (b) Map of height versus medial-lateral position for a band across the skull. (c) Overlay of the curvature obtained in panel b with a wide-field fluorescent image of a cross-section of the skull. The section was obtained by mechanically cutting the skull along the previous scanned path.

The topography across a desired region of a skull is mapped by successive measurements of the height of the skull with SHG metrology across a uniformly spaced grid. As a calibration with cadaver bone, a strip that spanned the full width of the skull was scanned in the sagittal plane with lateral step size of $200\ \mu\text{m}$ and axial resolution of $3\ \mu\text{m}$ (Fig. 2(b)). The surface of the skull exhibited an arc-like curve with a decrement of $\sim 1500\ \mu\text{m}$ in the Z-direction over the 10 mm lateral width. The accuracy of this measurement was assessed by comparing the SHG metrology data with an image of the skull. The cross-section of the same skull along the scanned region was obtained by embedding, mechanical cutting and then staining the bone with fluorescein dye. An overlay of the SHG contour map with the wide-field fluorescent image shows that the two measurements are in good agreement (Fig. 2(c)).

4. Osteotomy by plasma mediated laser ablation

The production of a thinned skull window in a living, anesthetized animal makes use of SHG metrology in both medial-lateral (X) and anterior-posterior (Y) directions to define the areal cutting path that follows the curvature of the skull. As an example, the height of a 2.0 mm by 2.0 mm region of the skull over the frontal cortex of mouse was mapped with SHG metrology at a $200\ \mu\text{m}$ lateral step size. The height varies by $\sim 700\ \mu\text{m}$ across the entire region (Fig. 3(a)). The data were fitted with splines, *i.e.*, cubic polynomials, and resampled at $5\ \mu\text{m}$ intervals to obtain a smooth surface that is used to drive the motorized stages for the ablation process (Fig. 3(b)).

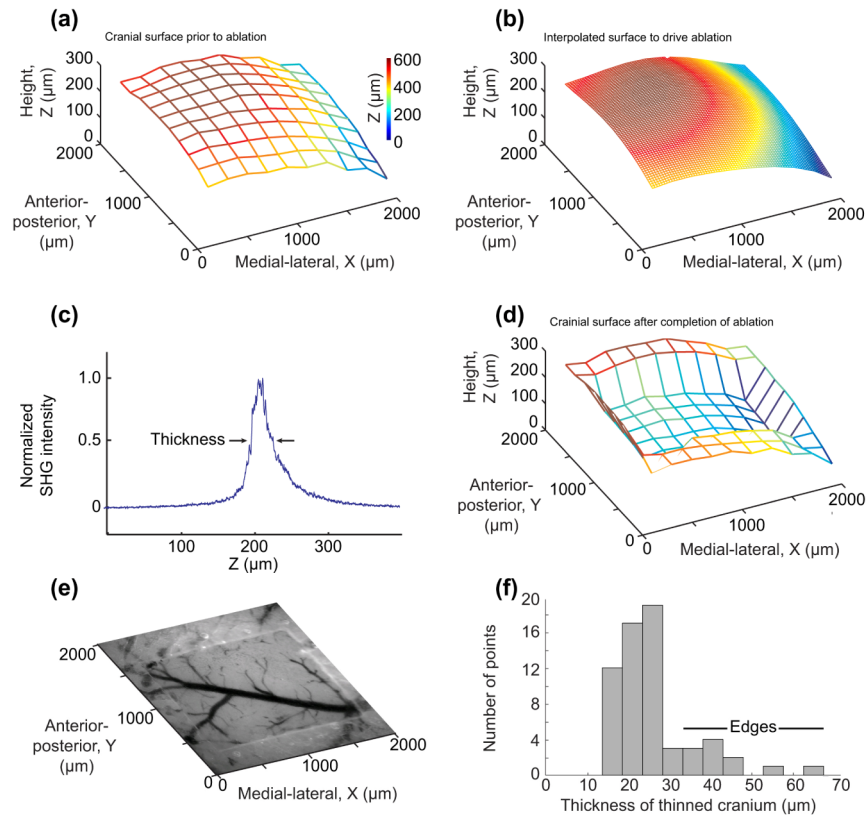


Fig. 3. Creation of a thinned skull by plasma-mediated laser ablation. (a) The intrinsic curvature of the skull was mapped over a 2 mm by 2 mm area with SHG metrology. (b) A smoothed version of the data in panel a that was used to calculate translational stage movements and shutter openings for thinning. (c) The decay in the SHG signal when the skull has been cut to within a thickness of 50 μm . Note the sharp fall-off in SHG signal at the interior surface of the skull compared with the signal from a thick skull (Fig. 2(a)). (d) The top surface of the thinned skull window measured with SHG metrology after completion of the ablation process. (e) Photomicrograph of the surface in panel d. (f) Histogram of the thickness obtained from measurements in panel d show the distribution of thicknesses; the points marked “Edges” are at the border of the window.

The skull is thinned in a grid-like pattern by steering the triple-axis translational stages along the measured surface curvature, with shutters synchronized to the stage movement to gate the amplified laser and metrology beams (Fig. 1(b)). Past work on the ablation of neuronal tissues guided the choice of ablation parameters [27]; the pulse energy is maintained at 3 μJ at the focus, the step size is 8 μm in the Y- and Z-directions, and the scan rate in the X-direction for the ablation process is chosen to be 8 mm/s, for which we deliver five ablation pulses per focal spot. As a surgical process, we first perform SHG metrology to define the front surface, then we iteratively cycle through six passes of ablation, to remove ~ 50 μm of bone, followed by SHG metrology. This cycle continues until the metrology indicates that the ablated region of the skull is 50 μm or thinner (Fig. 3(c)), after which ablation and metrology are interleaved one pass at a time until a final thickness of between 20 and 30 μm is achieved.

The data of Fig. 3 provides an example of a thinned skull window. The intact bone was systematically ablated in a 2.0 mm by 1.8 mm region until a ~ 350 μm deep region of bone was removed (Figs. 3(d) and 3(e)). The final thickness of the skull had a median value of 24 μm (Fig. 3(f)), which was within the range of thicknesses for a conventionally thinned skull window [3, 5]. At no point was the skull breached while ablating with feedback.

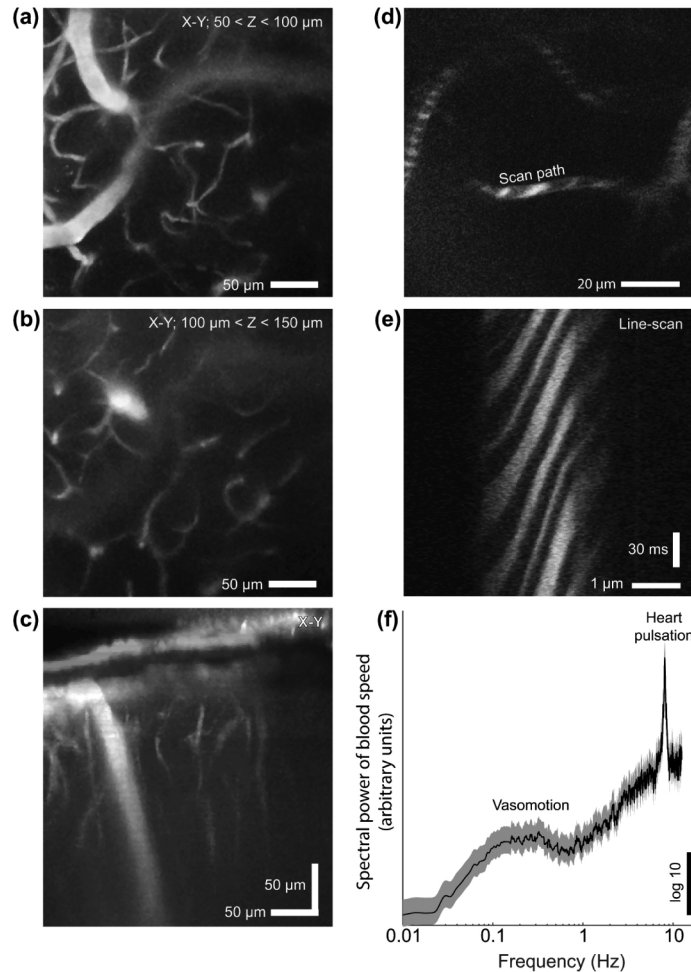


Fig. 4. *In vivo* two-photon laser scanning imaging demonstrates the utility of a laser ablated thinned skull window for functional imaging in mice. The blood plasma was stained with a high-molecular weight fluorescein-labeled dextran (2 MDa; Sigma). The window is above parietal cortex. (a) Maximum projection of a stack of images from a depth of 50 μm to 100 μm below the pia. The imaged area is 300 μm by 300 μm . (b) The same field as in panel a with a projection from 100 μm to 150 μm below the pia. (c) The stacks used for panels a and b were resliced to visualize the vessels along the optical axis. Note the penetrating vessels and fine microvessels. (d) A single microvessel that lies within the focal plane at a depth of 40 μm below the pia. The scan path lies along a straight section of the vessel that is used to track red blood cell flow. (e) Line-scan data from successive scans through the vessel in panel d. Individual red blood cells appear as dark streaks against the fluorescent blood plasma. The velocity of the flow is inversely proportional to the slope of the streaks. (f) Spectral power of the time series of the RBC speed in a vessel, located 80 μm below the pia, shows low frequency vasomotion broadly centred near 0.2 Hz and the heart rate at 8 Hz.

5. Two-photon functional imaging

Scattering from the thinned-skull transcranial window, realized here by laser ablation, must be minimized in ensure that the maximum imaging depth in brain tissue is achieved [3]. We used *in vivo* two-photon imaging of cortical vasculature and concurrent blood flow [30] to verify the optical quality of the window for functional imaging. The blood plasma was stained with fluorescein-conjugated-dextran to visualize the vascular lumen [29]. A 300 μm by 300 μm region within the confines of the window was imaged at 1 μm steps along the Z-direction

to obtain a volumetric stack. Maximum projections of 50 μm slabs along the Z-direction showed clean images of the labeled vasculature (Figs. 4(a) and 4(b)), while the projection of the images along the X-direction highlights the vertical extent of resolution, up to 200 μm deep in the pial surface here (Fig. 4(c)) and in general (3 mice).

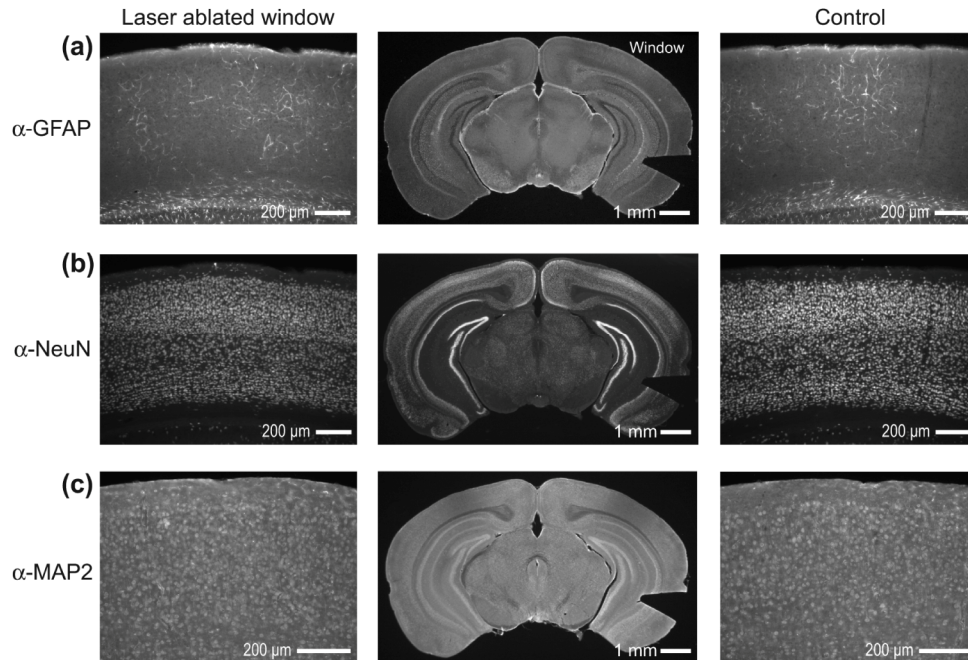


Fig. 5. Immunological assays of the viability of parietal cortex after laser ablation to create a transcranial window and functional imaging through the window. Alternate brain sections were stained with immunological markers to detect possible damage from the laser ablation and imaging. (a) Staining for reactive astrocytes with α -GFAP visualized with a fluorescent secondary antibody. The tissue under the thinned skull window had α -GFAP levels comparable to the contralateral control side. (b) Staining for the pan-neuronal marker α -NeuN, which labels essentially all neuronal nuclei. Both the window and control sides have comparable neuronal cell densities. (c) Staining for microtubules, as a test of neuronal integrity, with α -MAP2. The processes of the neurons are preserved for both the window and control sides of the section.

Functional imaging of the blood flow in an individual vessel was performed through the transcranial window. The brain is imaged, as above (Figs. 4(a)-4(c)), and a vessel that lies predominantly in a single focal plane is selected. A scan path is defined along the blood vessel and the beam is scanned along the vessel to form a sequence of line scans (Fig. 4(d)). Red blood cells appear as dark objects in the fluorescent plasma, so that a space-time plot formed from the line-scan data shows bands whose slope is inversely proportion to the speed of flow [29] (Fig. 4(e)). The velocity of the blood flow is automatically extracted [31]. A spectral analysis reveals two peaks (Fig. 4(f)); the peak at 8 Hz corresponds to the heart rate while that near 0.2 Hz corresponds to vasomotion [3, 32]. These data show that our automated osteometry procedure leaves the brain vascular healthy for an acute preparation (3 mice).

Immunohistochemistry was used to verify that the brain tissue was viable on a chronic basis. All tissue was derived from animals after both the plasma-mediated laser ablation to form the transcranial window and *in vivo* two-photon microscopy through the window, *i.e.*, after a period of 1 day. The animal was perfused and sectioned and immunohistochemical staining is carried out described [33]. Local tissue damage was assessed by testing for glial fibrillary acid protein (GFAP), a protein that proliferates in astrocytes under general conditions of physiological stress to gray matter [34]. Brain slices were reacted with α -GFAP as a marker to visualize glial activation (Fig. 5(a)). The region of the brain under the thinned

skull window showed that no significant labeling by comparison with the contra-lateral side. We further assessed the health of cortical tissue with the pan-neuronal marker α -NeuN, which binds to the nucleus and serves as an indicator of neuronal density [35], and the marker α -MAP2, which binds to microtubule associated protein and serves as an indicator of dendritic health [36]. The data show normal cell density (Fig. 5(b)) and viable primary and secondary dendrites (Fig. 5(c)) in comparison to the contra-lateral, untreated side of the brain (Figs. 5(b) and 5(c)). Thus tissue that was under the laser ablated thinned-skull window was histologically normal (5 sections per marker across 2 mice).

6. Summary and conclusion

We report the automated fabrication of a thinned-skull transcranial window in mice via the removal of bone by plasma-mediated ablation with ultrashort laser pulses (Fig. 3). This window permits *in vivo* imaging of the vasculature in the brain down to 200 μ m below the pial surface, as well as quantitative measurements of blood flow in individual microvessels (Fig. 4). The underlying brain tissue is completely viable after the surgery and imaging, as assayed by functional imaging (Fig. 4) and histological analysis (Fig. 5).

The speed of the current procedure is limited by the ablation process. The rate of ablation may be considerably increased with the additional use of temporal focused 100-fs laser pulses [37] to ablate the bone [25]. In this approach, the lateral extent of the pulse is decoupled from the axial extent to permit ablation of a “pancake”-shaped region. This allows the use of increasingly powerful lasers to ablate larger areas of bone at a constant thickness, although potential damage from the shock-wave of the ablation process will need to be investigated [38]. Finally, the speed of SHG metrology may be increased, should this be called for, by the use of temporally multiplexed, multi-focal beams [39, 40].

Automated surgery with plasma mediated ablation may be a critical tool for other aspects of experimental neuroscience. One application is the implantation of high density arrays of microelectrodes [41] or microoptrodes [42], in which an array of one hundred or more microelectrodes is pressed into the brain. Currently a single craniotomy is prepared that encompasses all electrodes. This results in considerable weakening of the skull and provides a potential path for infection. An alternative procedure is to use plasma-mediated laser ablation to machine a corresponding lattice of holes in the skull and implant the array of microelectrodes directly through these holes [26]. Second harmonic generation can be used to control the cutting and confirm the depth of the holes. In addition, laser induced plasma spectroscopy [43] may be used for the identification of bone versus soft tissue [44] as a means to avoid damage to the dura.

Acknowledgments

We thank Andy Y. Shih for assistance with the blood flow measurements, Allan Schweitzer for assistance with the electronics and programming, Christopher Bergeron and Jeffrey A. Squier for technical discussions, and Céline Mateo for comments on the manuscript. This work was generously supported by a grant from the NIBIB (1EB003832).